A3 CRYSTAL GROWTH DYNAMICS

A3.1.1 Study of Crystal Growth During 2 °C/hr Dynamic Crystallization Experiments

Growth of an individual crystal cannot be visually tracked over the course of a controlled cooling experiment, but representative snapshots of crystallization progress during the thermal history of this study were obtained by stopping runs and quenching the run products at intermediate time points. Figure A3.1 shows charges from composition 2b-1 that were stopped at three separate times: (a) was quenched immediately after the completion of the first 2 °C/hr cooling step, (b) after the 24 hr hold interval in the middle of the run between the two cooling steps, and (c) immediately after the second 2 °C/hr cooling step. These images confirmed that crystallization had commenced prior to the intermediate 24 hour hold interval, which likely prevented major amounts of delayed nucleation and any resulting rapid disequilibrium growth, as discussed in Section 2.2.5, from influencing the bulk of the crystal formation or the rim compositions.

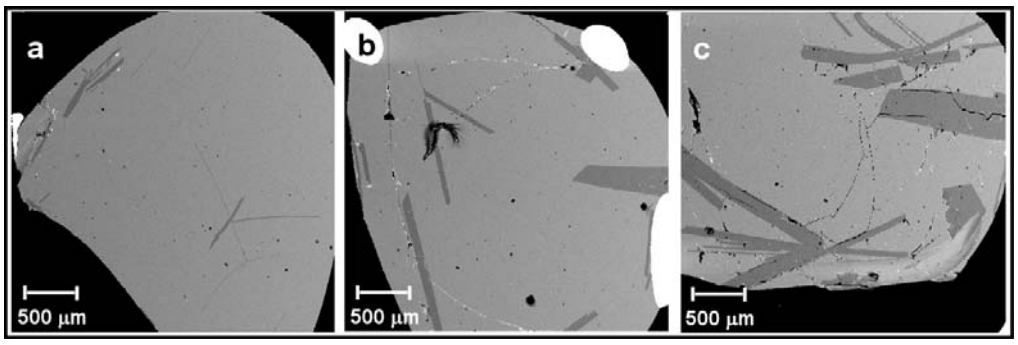

Figure A3.1. Representative BSE crystal images (2b-1-3, 2b-1-4, 2b-1-5) quenched at three intermediate time points (a) 20.5, (b) 44.5, and (c) 67 hours during the controlled cooling thermal regime of this study

A3.1.2 Glass Composition Evolution During Dynamic Crystallization Experiments

Average compositions based on random data points throughout the sample glass are reported for the initial fused compositions (Table A3.1); the three intermediate times of 20.5, 44.5, and 67 hours (Table A3.2); and the final melt composition at 96 hours (Table A3.3). These times represent the inflection points on the thermal history shown in Figure A1.2 both before and after controlled cooling intervals. Points for Table A3.2 were only analyzed for major elements Ca, Mg, Al, and Si, but the analytical conditions were the same as described in Section A1.3 for the major element transect analyses of the anorthite crystals. Analytical conditions for the initial and final melt compositions are given in Section 2.2.4.

Table A3.1. Starting compositions of glasses fused for three hours as analyzed by electron microprobe. 1 σ standard deviation uncertainty is shown in parentheses and applies to the final digit of each value.

	2b-1-1 n = 10	2b-2-1 n =10	2b-3-1 n =10	2b-4-1 n =10	2b-5-1 n =10	2b-6-1 n =10	2b-7-1 n =10
SiO_2	46.6 (2)	46.79 (9)	46.6 (2)	46.4 (2)	45.8 (3)	45.9 (2)	46.0 (1)
Al_2O_3	21.56 (6)	21.79 (5)	22.15 (5)	22.56 (7)	23.07 (7)	24.02 (6)	25.44 (9)
MgO	0.99 (2)	2.57 (5)	4.30 (5)	5.9 (1)	7.78 (8)	9.2 (2)	10.1 (1)
CaO	30.26 (7)	28.4 (1)	26.46 (7)	24.4 (1)	22.41 (8)	20.37 (9)	18.35 (9)
SrO	0.13 (3)	0.13 (3)	0.14 (4)	0.13 (3)	0.13 (3)	0.15 (3)	0.12 (3)
BaO	0.50 (8)	0.5 (1)	0.49 (4)	0.51 (7)	0.53 (6)	0.52 (6)	0.54 (9)
Na_2O	0.01 (1)	0.02 (1)	0.02 (1)	0.01 (1)	0.02 (1)	0.02 (1)	0.01 (1)
K_2O	0.023 (5)	0.025 (5)	0.023 (6)	0.023 (6)	0.025 (7)	0.022 (8)	Na
	100.07	100.23	100.10	99.93	99.77	100.20	100.56

na = not analyzed

Table A3.2. Major element glass compositions analyzed by EMP at three intermediate time steps along the dynamic crystallization path of Figure A1.2. 1 σ standard deviation of the analyses (not error of mean) is shown in parentheses and applies to the final digit of each value.

	20.5 hours			44.5 hours			67 hours		
	2b-1-3 n = 30	2b-4-3 n =30	2b-7-3 n =30	2b-1-4 n =30	2b-4-4 n =30	2b-7-4 n =30	2b-1-5 n =30	2b-4-5 N =30	2b-7-5 n =30
SiO_2	47.3 (2)	47.1 (2)	45.9 (3)	47.7 (2)	47.6 (3)	46.1 (3)	48.0 (3)	48.0 (3)	46.6 (3)
Al_2O_3	21.2 (2)	21.9 (2)	24.4 (2)	20.5 (1)	20.40 (7)	23.40 (6)	18.5 (3)	18.3 (1)	21.2 (2)
MgO	0.99 (2)	6.05 (7)	10.6 (1)	1.01 (2)	6.62 (6)	11.79 (7)	1.14 (3)	7.50 (7)	13.6 (1)
CaO	30.5 (1)	24.54 (8)	18.35 (9)	30.8 (1)	25.04 (7)	18.10 (7)	32.4 (1)	25.71 (9)	17.82 (6)
	99.99	99.59	99.25	100.01	99.66	99.39	100.04	99.51	99.22

Table A3.3. Final melt compositions after 96.5 hours from EMP analyses of glass points distributed throughout melt. 1 σ standard deviation uncertainty is shown in parentheses and applies to the final digit of each value. Note that these runs were held for 30 hours at the final temperature.

	2b-1-2 n = 10	2b-2-2 n =10	2b-3-2 n =10	2b-4-2 n =10	2b-5-2 n =10	2b-6-2 n =10	2b-7-2 n =10
SiO_2	48.0 (1)	47.4 (3)	47.86 (9)	47.6 (3)	46.3 (3)	46.3 (3)	46.4 (1)
Al_2O_3	18.14 (9)	17.8 (1)	17.9 (2)	18.03 (8)	18.80 (7)	19.8 (1)	20.97 (6)
MgO	1.17 (2)	3.24 (4)	5.5 (1)	7.8 (1)	10.40 (8)	12.2 (2)	14.2 (2)
CaO	32.5 (2)	30.7 (1)	28.1 (1)	25.9 (1)	23.20 (8)	20.25 (5)	17.6 (1)
SrO	0.13 (3)	0.14 (3)	0.14 (3)	0.14 (3)	0.11 (2)	0.14 (3)	0.13 (3)
BaO	0.63 (9)	0.57 (8)	0.61 (9)	0.64 (6)	0.66 (4)	0.71 (6)	0.65 (7)
Na_2O	0.01 (1)	0.02 (1)	0.02 (1)	0.02 (1)	0.02 (1)	0.02 (1)	0.02 (1)
K_2O	0.021 (6)	0.019 (7)	na	0.026 (7)	0.023 (5)	na	Na
	100.60	99.89	100.13	100.16	99.51	99.42	99.97

na = not analyzed

The fraction of crystal growth for compositions 2b-1, 2b-4, and 2b-7 quenched at each time step shown in Figure A3.1 was calculated from the evolving melt compositions according to the fractional crystallization equation,

$$\boldsymbol{C_{i(l)} = C_{o(l)}(1\text{-}F)^{(D\text{-}1)}}, \qquad \text{(A2)}$$

where the final composition of the liquid C_i is a function of the initial liquid concentration (C_o), the fraction crystallized (F), and the bulk partition coefficient

between the solid and liquid phases (*D*). The amounts of crystallization for the least magnesian (2b-1), most magnesian (2b-7), and an intermediate (2b-4) composition at five time points along the controlled cooling path of the experiments is shown in Figure A3.2.

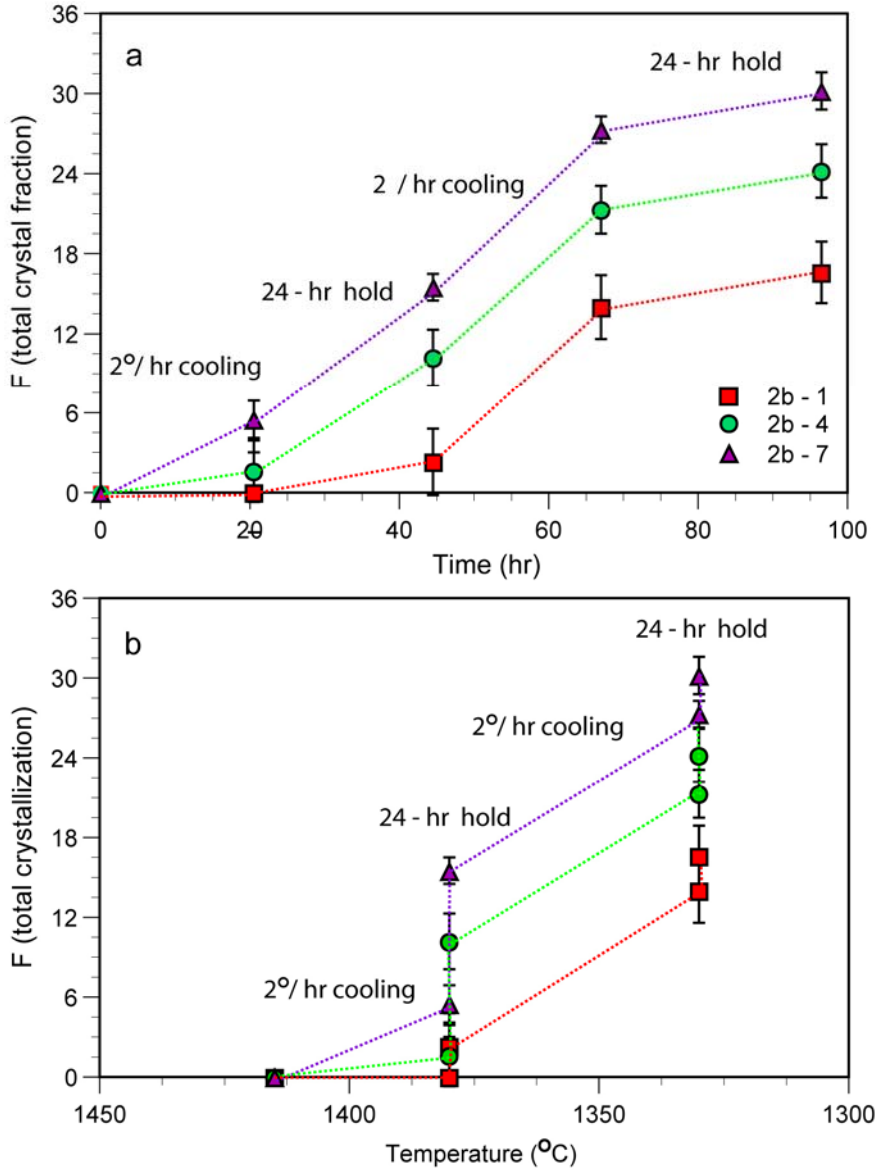

Figure A3.2. Calculated crystal fraction increases during the controlled cooling experiments for compositions 2b-1 (least magnesian), 2b-4, and 2b-7 (most magnesian) over ~100 hours as a function of (a) time and (b) temperature.

Plot (a) shows the progress of crystallization as a function of time spent in the furnace, and (b) represents the overall fraction of crystallization as a function of temperature, where crystallization occurring during isothermal periods appears as discontinuous jumps. MgO partition coefficients were used to calculate *F* since the differences in *F* generated by approximating apparent *D* values using initial vs. final melt compositions are small. Uncertainty in crystallization (1 σ) was generally less than 0.03 of the fraction crystallized.

While extent of crystallization at each temperature is clearly different for each composition, with the least magnesian composition crystallizing less than the most magnesian, no large increase in crystallization between 67 and 96 hours is observed within error, as expected if crystal growth is continuous and does not lag as cooling proceeds. This offers some confidence that the systems are not rapidly growing crystals that are clearly out of equilibrium with their surrounding melts.

A3.1.3 Melt Homogeneity During Controlled Cooling Experiments

Alternating intervals of controlled cooling with 24 hr isothermal periods in the thermal program shown in Figure A1.2 were designed to slow crystallization progress over the course of experiments and avoid rapidly growing crystals significantly out of equilibrium with the coexisting melt phase. It was expected that crystallization would produce liquid inhomogeneities, and allowing the melts to rehomogenize during isothermal periods eliminates the need to select from varying final liquid composition data a particular composition to use with crystal rim data in calculating partition

coefficients. Analyzing major element glass contents of samples quenched at specific time points during a typical controlled cooling experiment offers an opportunity to evaluate the extent of liquid heterogeneities produced and how effectively diffusion during 24 hr isothermal holding removes them at the temperatures of this study.

To track global melt composition variations, we developed a heterogeneity index (HI) defined as HI = (1 σ of 10-30 random melt points)/(1 σ analytical error), reported as %. The standard deviations of glass major element composition data (Table A3.1 through A3.3) have been divided by the average instrumental counting statistics uncertainties for the analyses. Analytical error is calculated from the raw X-ray count electron microprobe data according to the following equation reported in (Kremser):

$$\varepsilon_{P-B} = \sqrt{\frac{N_P}{t_P^2} + \frac{N_B}{t_B^2}} \Big/ \left(\frac{N_P}{t_P} - \frac{N_B}{t_B} \right), \qquad \text{(A3)}$$

where N_P is the total number of on-peak counts, N_B the total number of background counts, t_P the on-peak count time, and t_B the background count time. HI values < 2 indicate a homogeneous material.

Plots of melt heterogeneity at the various time steps of the dynamic crystallization thermal regime described earlier in this section are shown for compositions 2b-1, 2b-4, and 2b-7 in Figure A3.3. Time = 20.5 hours represents quenching after the first 2 °/hr controlled cooling period, time = 44.5 hours was quenched after the first 24 hr hold at ~1380 °C, 67 hours = immediately after the second 2 °/hr controlled cooling period, and a final 30 hr hold (minimum of 24 hours for this step) was completed after 96 hours. CaO remains relatively homogeneous throughout the experiments, whereas Al_2O_3 exhibits the greatest variations in melt composition with peaks corresponding to times immediately after intervals of 2 °/hr reductions in temperature, as discussed above. Generally, the

Al_2O_3 inhomogeneities caused by crystallization present after 20.5 and 67 hours were removed by the isothermal periods completed at 44.5 and 96 hours. For all other elements, diffusion and/or convection efficiently erased heterogeneities as they were produced by crystallization. Other non-systematic variations present between the three melt compositions are interpreted as small (% level) inhomogeneities. Since 1 σ ratios are compared here, $0.5 < HI < 2$ are not considered significant.

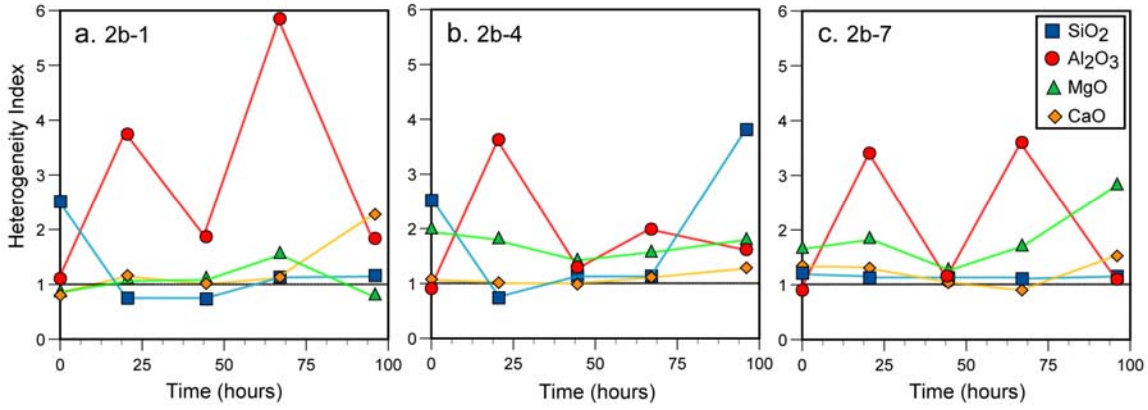

Figure A3.3. Heterogeneity index (HI) for melt major element oxide contents for compositions (a) 2b-1, (b) 2b-4, and (c) 2b-7 as a function of time in the controlled cooling program, where HI = % 1 σ of 10-30 random melt points/ % 1 σ analytical error.

MgO heterogeneities are less pronounced but appear related to those of Al_2O_3, perhaps indicating a charge-compensating role for Mg^{2+} near Al^{3+} complexes in the melt structure. SiO_2 data are generally less precise than that of the other major oxides despite silica abundance, so differences in analytical error and compositional uncertainty arising from glass heterogeneity are less resolved. The HI values of Figure A3.3 show either little SiO_2 variation in the melts or, in the case of panel (b), apparently significant heterogeneity at 0 hours and 96 hours due to a combination of 70 % lower analytical error for those analyses and smaller number of analyses (10) than at 20.5, 44.5, and 67 hours

(30). Given that Si, as a network-former in melts, likely diffuses more slowly than Ca or Mg, the HI at times 0 and 96 may be better representations of general SiO_2 heterogeneity in these experiments than the HI calculated for the intermediate times.

Table A3.4 provides another view of Al_2O_3 heterogeneity development over the course of a typical controlled cooling experiment in this study. Al_2O_3 standard deviations exceed the instrumental error (0.3 % relative) after cooling intervals and return close to analytical uncertainty after the isothermal periods. The progressive return of Al_2O_3 variations to within analytical uncertainty at time = 96.5 hours as a function of melt major element composition (0.50, 0.44, 0.29 from least magnesian to most magnesian) suggests that diffusion rates may be higher in more magnesian compositions..

Table A3.4. Comparison of Al homogeneity in melt at time steps plotted in Figure A3.2. Typical analytical error (√(avg counts) as % avg.) for Al_2O_3 is 0.3 %.

Experiment #	Time in furnace (hrs)	Melt Al_2O_3 Average wt. %	1 σ as % avg.
2b-1-1	Fuse (3)	21.56 (6)	0.28
2b-1-3	20.5	21.2 (2)	0.94
2b-1-4	44.5	20.5 (1)	0.49
2b-1-5	67	18.5 (3)	1.62
2b-1-2	96.5	18.14 (9)	0.50
2b-4-1	Fuse (3)	22.56 (7)	0.31
2b-4-3	20.5	21.9 (2)	0.91
2b-4-4	44.5	20.40 (7)	0.34
2b-4-5	67	18.3 (1)	0.55
2b-4-2	96.5	18.03 (8)	0.44
2b-7-1	Fuse (3)	25.44 (9)	0.35
2b-7-3	20.5	24.4 (2)	0.82
2b-7-4	44.5	23.40 (6)	0.26
2b-7-5	67	21.2 (2)	0.94
2b-7-2	96.5	20.97 (6)	0.29

These results indicate that except for Al_2O_3 even random melt points some distance from the anorthite crystals do not show any measurable degree of compositional variation 67

hours into the thermal program, when the furnace stops at a final temperature and anorthite crystallization apparently ceases.

A3.2 Near-Crystal Melt Homogeneity Test

Two dimensional compositional maps similar to those described in Section 2.2.4 for the anorthite crystals were analyzed for MgO, SrO, and BaO. The samples were 2b-1-5, 2b-4-5, and 2b-7-5, which had been quenched after 67 hours (Table A3.2). Analytical conditions were identical to those of Section 2.2.4 except that since most of analyses were on glass, the beam current was reduced to from 400 to 200 nA. The trace element grids extended from the outermost crystal edges approximately 100 μm into the melt, perpendicular to the crystal-melt interface. Two grids per sample were analyzed and their locations are shown in Figure A3.4. Polygonal point data for MgO, SrO, and BaO are reported in wt. % and crystal boundaries and summary transects were constructed as described in Section A2.2 for the anorthite 2-D compositional maps.

Figure A3.5 of 2b-1-2 melt grids shows a possible very slight elevation in MgO and BaO in the glass nearest the crystal-melt interface in (a) and (c), but this variation is not statistically significant in the summary transects of (d), and the melt grid data in the right column indicate no systematic concentration gradients parallel to the crystal edge. Little evidence of growth-related melt composition gradients exists for sample 2b-4-5 (Figure A3.6), though some MgO heterogeneity perpendicular to the interface is shown in (e) of that figure. The clearest demonstration of melt concentration gradients produced by crystal growth are found around anorthite laths in composition 2b-7, where MgO melt

contents in both (a) and (e) are elevated 1–7% near the crystal-melt interface relative to those of glass analyses 15–20 μm further away. SrO and BaO contents show no variation, though in all six melt grids analyzed it is possible, and even likely, that trace element concentration gradients exist within 5 μm of the interface below the spatial resolution of the electron beam. Improvements in quantitative TEM EDS technology may make these regions accessible to further study.

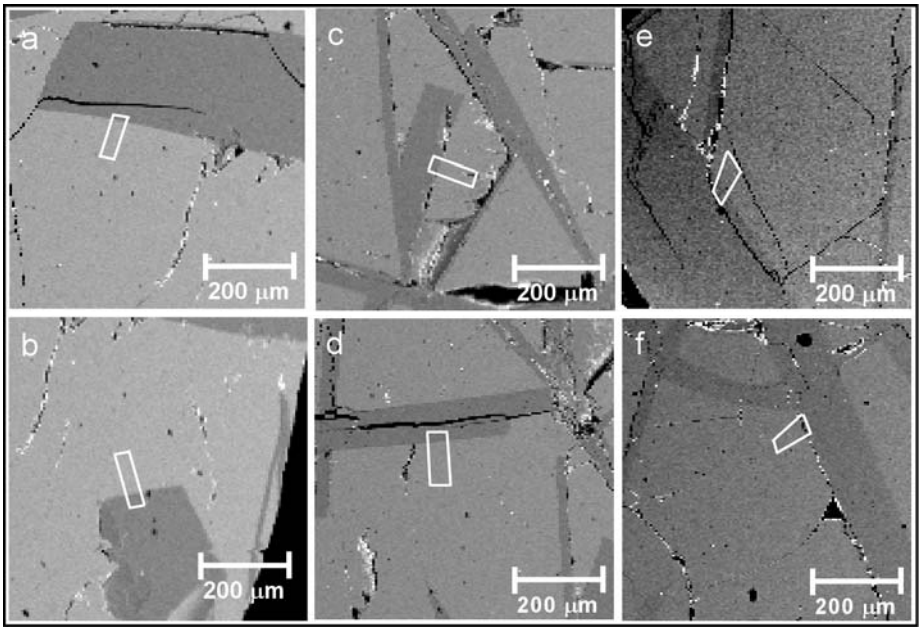

Figure A3.4. BSE imaging of melt grid locations for runs quenched 67 hours into a controlled cooling experiment of the thermal regime shown in Figure A1.2. (a) and (b): sample 2b-1-5, (c) and (d): sample 2b-4-5, and (e) and (f): sample 2b-7-5.

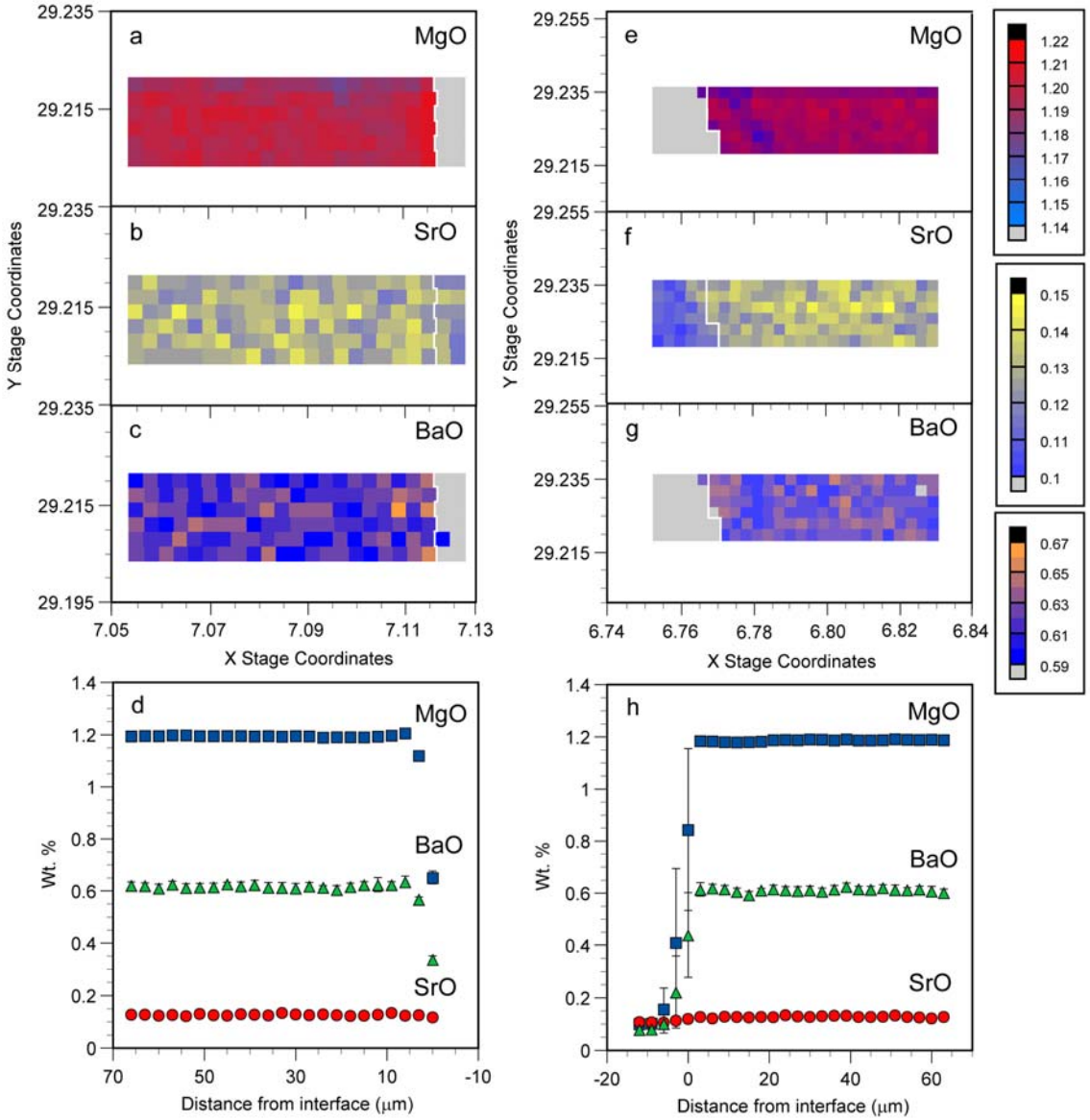

Figure A3.5. Sample 2b-1-5: Two grid melt maps of MgO, SrO, BaO wt. % data and summary transect for each grid.

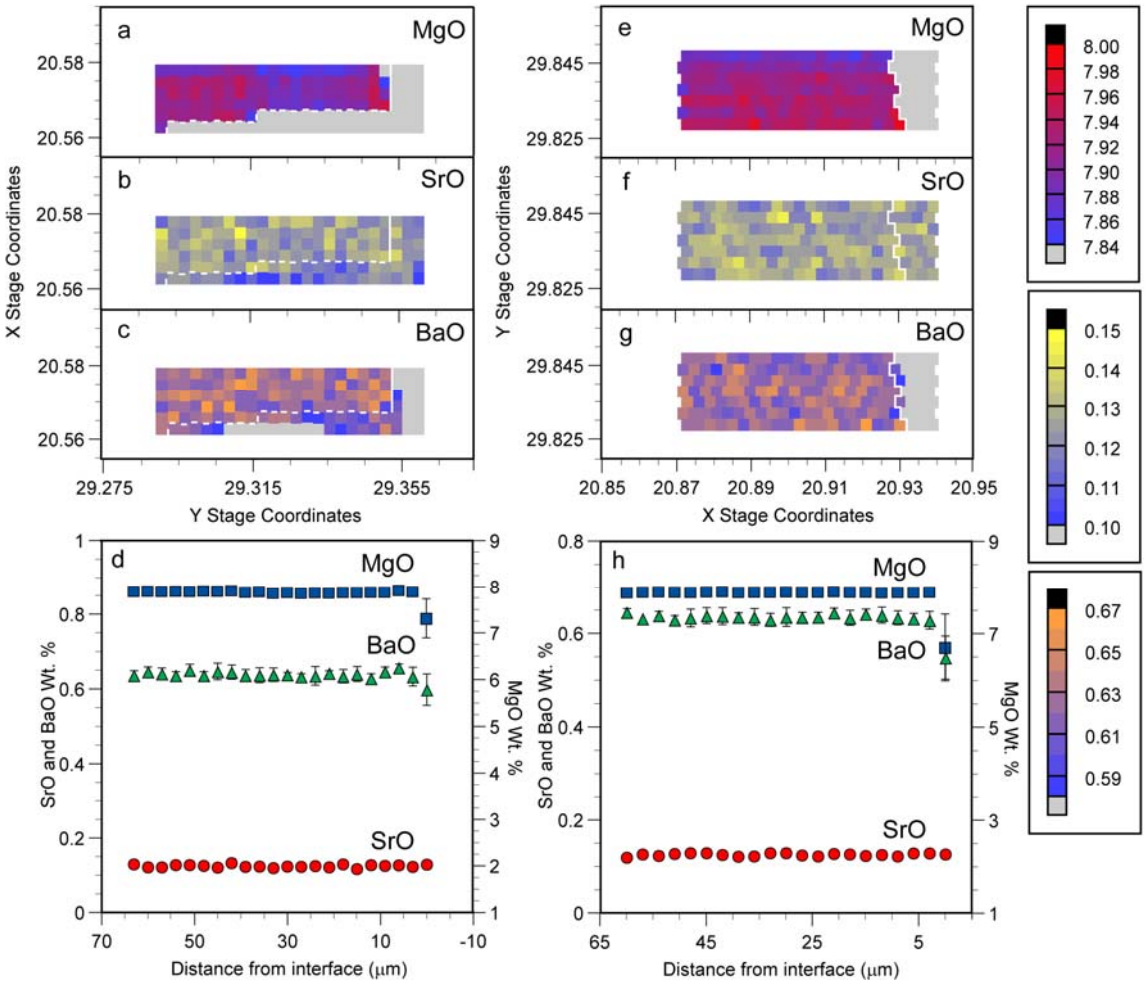

Figure A3.6. Sample 2b-4-5: Two grid melt maps of MgO, SrO, BaO wt. % data and summary transect for each grid.

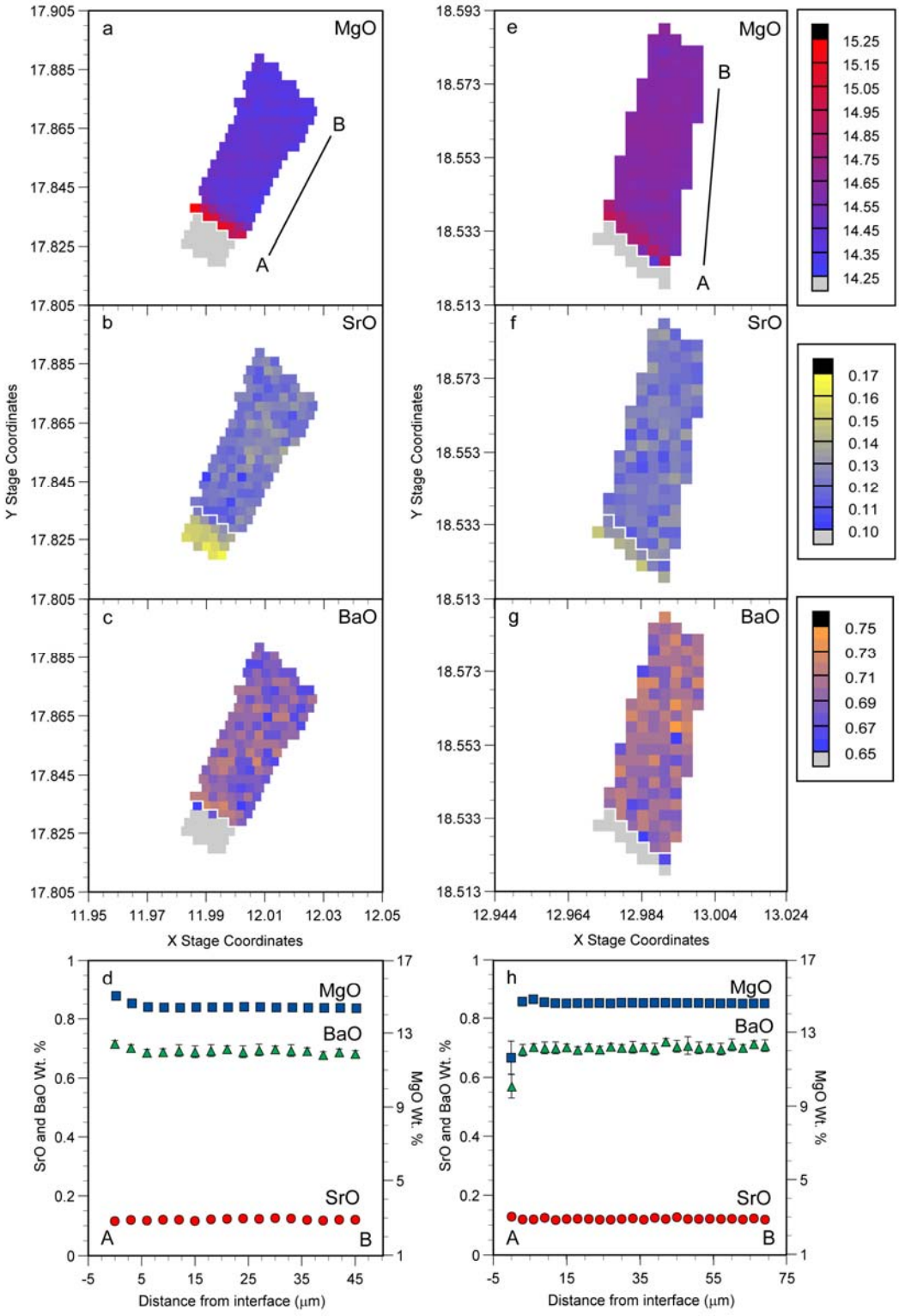

Figure A3.7. Sample 2b-7-5: Two grid melt maps of MgO, SrO, BaO wt. % data and summary transect for each grid.

A3.3 Effects of Crystal Growth Rate on Partitioning: Rapid (20 °/hr) Controlled Cooling Partitioning Study and Crystal Growth Dynamics

Rapid crystal growth can significantly influence apparent partition coefficients by incorporating elevated amounts of slow-diffusing incompatible trace elements into the crystal structure. When the time necessary to fully equilibrate crystal contents with the surrounding melt exceeds experimental feasibility, consideration of crystal growth effects on partitioning in the specific system(s) of interest becomes important. This section compares partition coefficients obtained by the controlled cooling thermal regime shown in Figure A1.2, which consisted of isothermal intervals and two 2 °C/hr cooling steps, and partition coefficients calculated for experimental runs in which crystals were grown by reducing the furnace temperature by 20 °C/hr to approximately the same final temperature as the 2 °C/hr cooling runs. The 20 °C/hr cooling experiments (2b-1-7, 2b-4-7, 2b-7-9) included no isothermal intervals and total run durations were 5-6 hours, as shown in Table A6.1.

A3.3.1 Compositional Data for Rapid Growth (20 °C/hr Cooling) Experiments

Trace element contents of the anorthite crystals and surrounding glass from the 20 °C/hr cooling experiments were obtained according to the methods detailed in Section 2.2.4 and A2.1, except these samples were analyzed using the new Caltech JEOL JXA-8200 electron microprobe. The analytical error associated with single point analyses of anorthite and glass MgO, SrO, and BaO contents are reported in Table A3.5. Average instrumental errors for data from the intermediate composition 2b-4 are represented by experiment 2b-4-2 data, measured using the older JEOL 733 electron microprobe, and

2b-4-7 using the new JEOL JXA-8200. MgO and SrO instrumental error is similar for both probes, but the JEOL JXA-8200 detected higher count rates in the Lα LiF crystal X-ray line region for Ba, producing better BaO data.

Table A3.5. Percent analytical error for anorthite and glass trace elements analyzed on the new JEOL JXA-8200 electron microprobe compared to that on the older JEOL 733 model.

	MgO	SrO	BaO
2b-4-2 with JEOL 733			
Anorthite:	0.4	3.5	7.1
Glass:	0.07	3.3	1.6
2b-4-7 with JEOL JXA-8200			
Anorthite:	0.4	3.2	4.1
Glass:	0.07	3.3	0.9

Locations of the 2-D polygonal analysis grids for the three 20 °C/hr cooling experiment samples are shown in Figure A3.8.

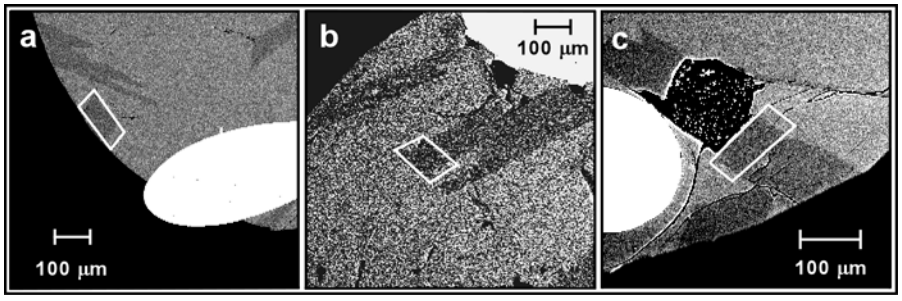

Figure A3.8. BSE imaging of 2-D compositional mapping grids (outlined in white) for trace element (MgO, SrO, BaO) analysis of 20 °C/hr cooling experiments: (a) 2b-1-7, (b) 2b-4-7, and (c) 2b-7-9.

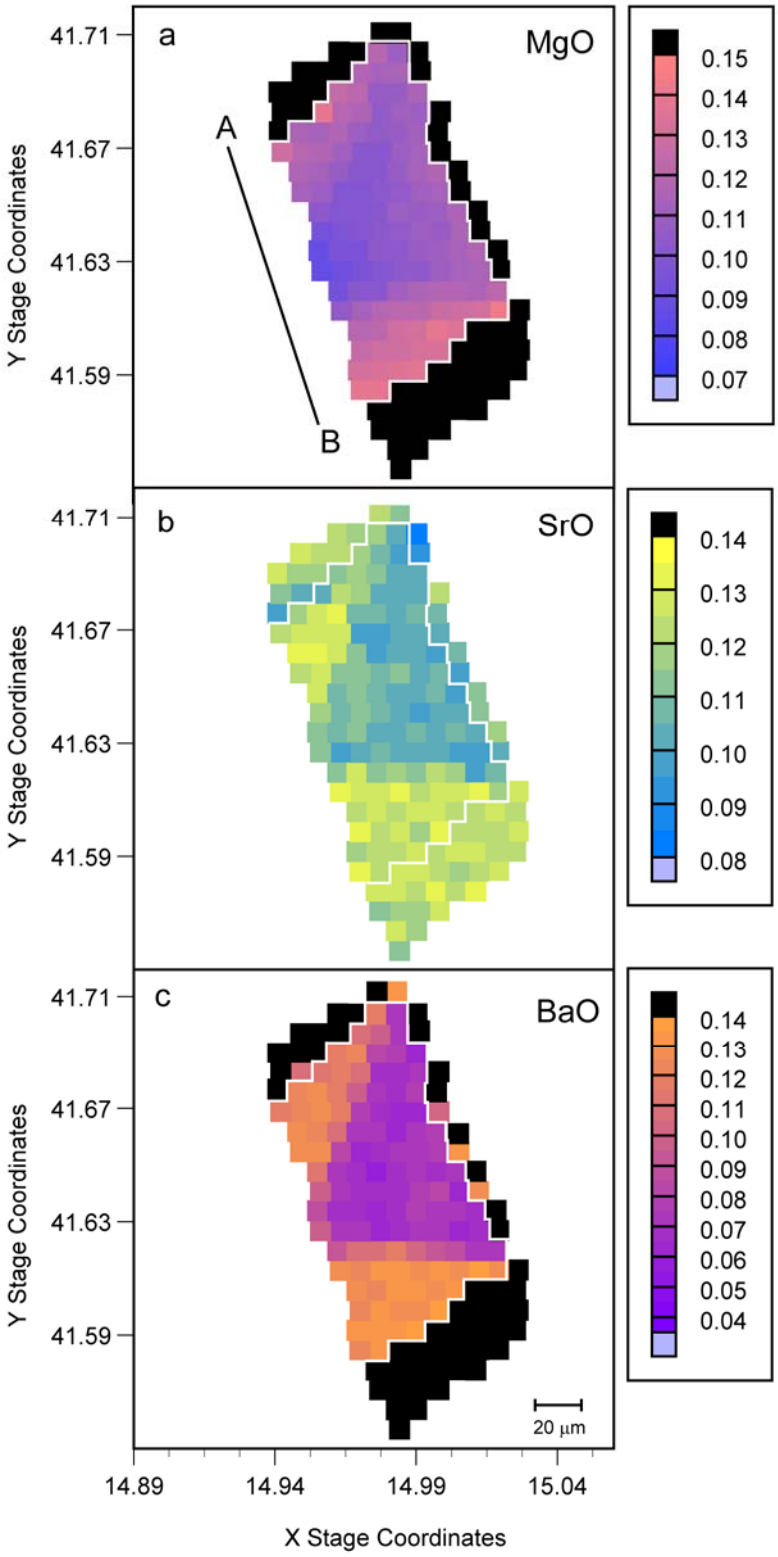

Figure A3.9. Sample 2b-1-7 (a) MgO, (b) SrO, (c) BaO maps (wt. %).

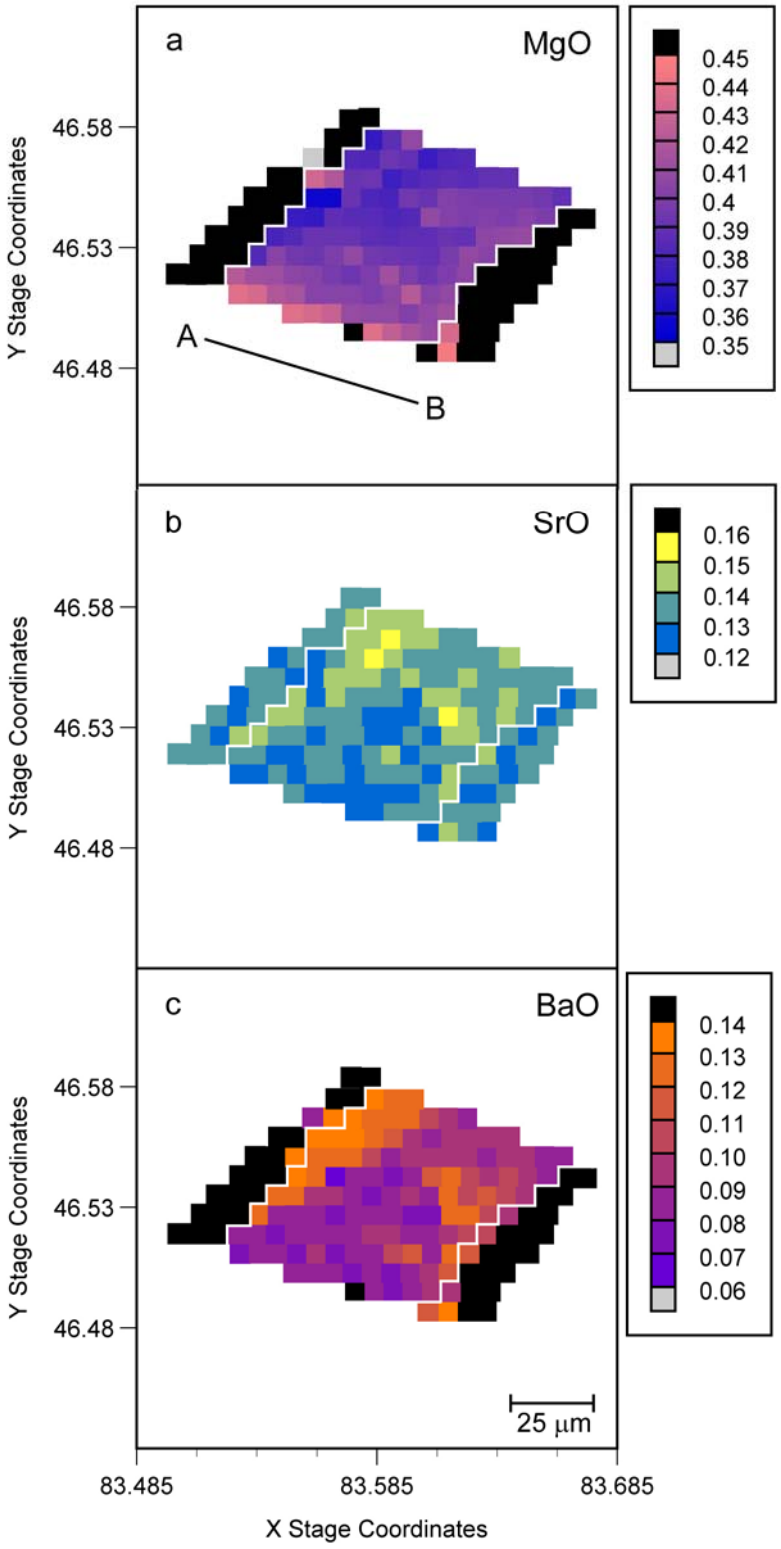

Figure A3.10. Sample 2b-4-7 (a) MgO, (b) SrO, (c) BaO maps (wt. %).

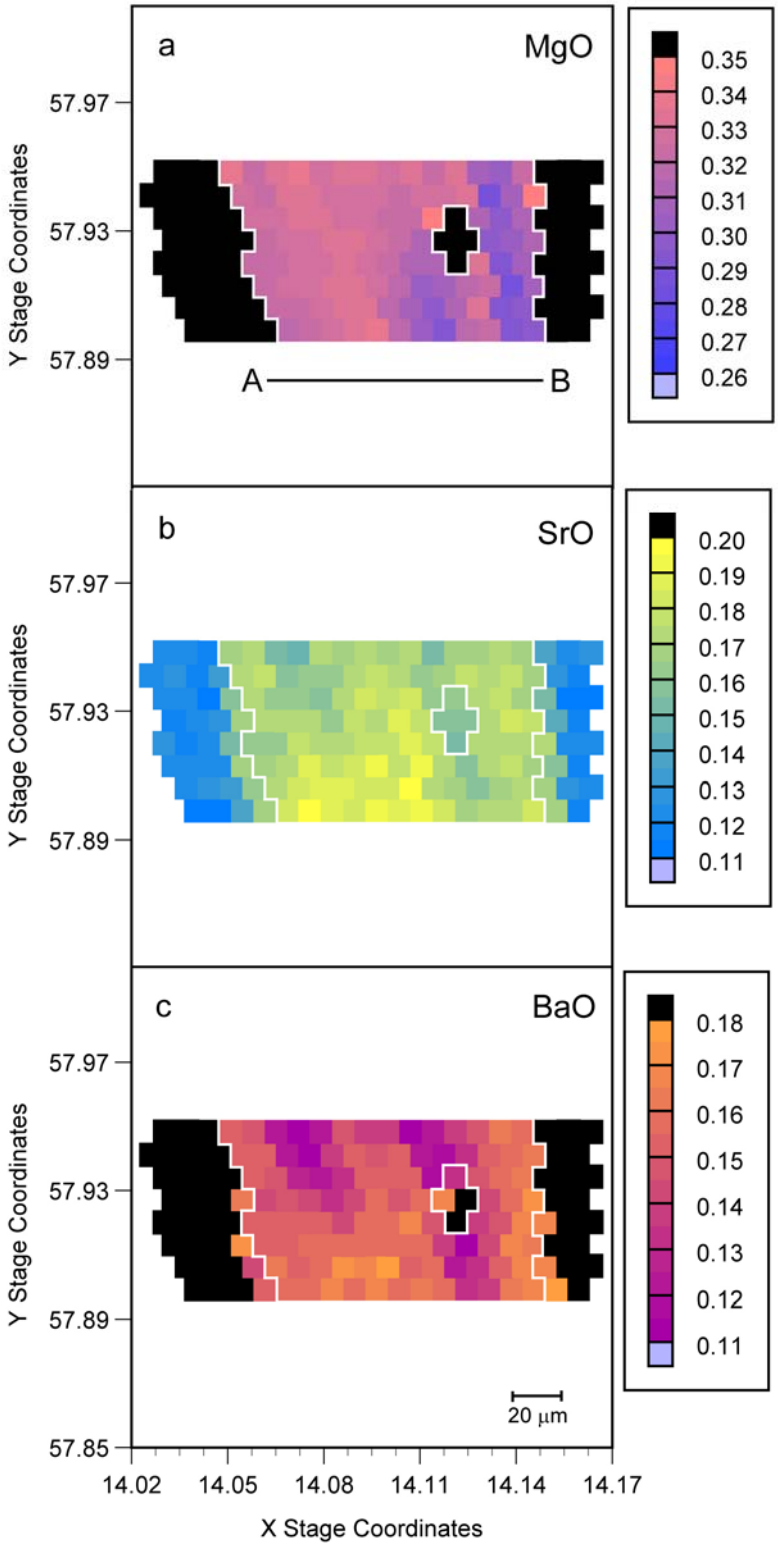

Figure A3.11. Sample 2b-7-9 (a) MgO, (b) SrO, (c) BaO maps (wt. %)

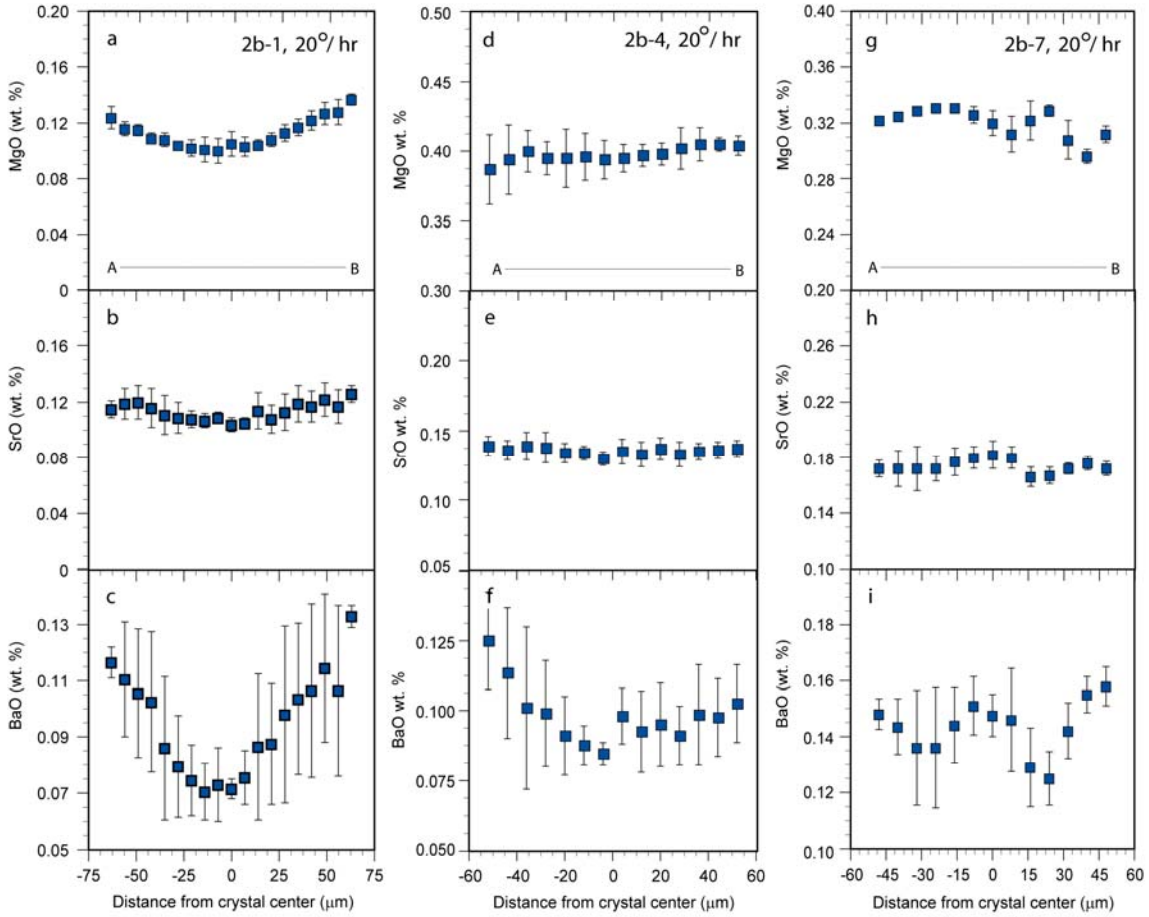

Figure A3.12. Trace element summary transects from grid data of 2b-1-7, 2b-4-7, and 2b-7-9.

Maps of individual wt. % data points for MgO, SrO, and BaO are given in Figures A3.9, A3.10, and A3.11 for sample charges 2b-1-7, 2b-4-7, and 2b-7-9, respectively. Summary transects across the crystals (rim to rim) that average data rows perpendicular to the A-B lines shown on the map figures are plotted in Figure A3.12. Note that summary transects suppress some compositional structure resulting from sector zoning.

The 20 °C/hr cooling experiment trace element data reveal formation of distinct sector zoning in 2b-1-7 and 2b-4-7, particularly in the SrO and BaO data, that was not

apparent in the maps of crystals grown under 2 °C/hr conditions. Composition 2b-7 may also be capable of producing crystals with this classic kinetic disequilibrium feature; 2b-7-9 composition maps (Figure A3.11) show clear variations in trace element distributions but the availability of well-formed, semi-equant laths in the polished cross section of the sample, which would have been better candidates for observing sector zoning, was limited.

Table A3.6 below summarizes molar partitioning data for trace elements Mg, Sr, and Ba from quantitative electron microprobe mapping of most equant crystals and surrounding glass from runs 2b-1-2 and 2b-1-2 (2 °C/hr cooling) and runs 2b-1-7 and 2b-7-9 (20 °C/hr) cooling. Partition coefficients are calculated from the crystal rim data and the adjacent glass. Composition 2b-1 starting material has the least magnesium (~1 wt. %) and 2b-7 has the most (~12 wt. %). Numbers in parentheses are 1 σ uncertainties on the final digit of each value.

Table A3.6. Comparison of 20 °C/hr to 2 °C/hr Mg, Sr, Ba D rim values for 2b-1, 2b-4, and 2b-7.

2b-1		2 °C/hr	20 °C/hr
	D^{mol}_{MgO}	0.091 (5)	0.120 (8)
	D^{mol}_{SrO}	0.90 (5)	1.02 (7)
	D^{mol}_{BaO}	0.18 (2)	0.25 (1)
2b-4			
	D^{mol}_{MgO}	0.052 (4)	0.058 (2)
	D^{mol}_{SrO}	1.06 (5)	1.19 (6)
	D^{mol}_{BaO}	0.18 (2)	0.21 (3)
2b-7			
	D^{mol}_{MgO}	0.029 (1)	0.027 (1)
	D^{mol}_{SrO}	1.45 (6)	1.66 (9)
	D^{mol}_{Bao}	0.21 (2)	0.29 (1)

D^{mol} values of the 20 °C/hr cooling experiments are slightly elevated relative to those of the 2 °C/hr cooling runs, and this proportional elevation appears correlated with ionic radius, in particular in composition 2b-7, which shows no difference in D^{mol}_{MgO} but some for SrO and BaO. It should be noted that the partition coefficients reported in Table A3.5 represent the maximum observed effect the 20 °C/hr cooling rate could have on apparent partitioning behavior, since in the case of 2b-1-7 and 2b-4-7 composition data from the edges with the highest trace element abundances were used to calculate the *D* values shown. If those sectors grow before the sector(s) with lower trace element contents, the latter may represent the true crystal contents grown in closer equilibrium with the surrounding melt and the *D* values will be closer to those calculated from the 2 °C/hr cooling experiments. Either way, a significantly more pronounced effect on partition coefficients with cooling rate was observed by LaTourrette (1993) for U and Th clinopyroxene-melt partition coefficients (fO_2 = QFM), as shown in Table A3.7.

Table A3.7. Clinopyroxene-melt D_U and D_{Th} for experiments cooled at 0.1 °C/hr and 1.7 °C/hr (LaTourrette, 1993).

D2-TUBAS		0.1 °C/hr	1.7 °C/hr
	D_U	0.0033 (3)	0.0058 (8)
	D_{Th}	0.0069 (8)	0.0120 (15)

The D2-TUBAS partition coefficients are averages of 2-3 crystals because they derive from fission (^{235}U) and alpha (^{230}Th) track counting within crystal interior areas at least 20 μm from the edges, and thus each crystal represents one measurement of trace

element concentration in the solid phase. The differences in U and Th *D* values due to a factor of ~20 in cooling rate resulted in a doubling of the partition coefficients, which is a significantly greater effect than we observe for the alkaline earths in our experiments.

A3.3.2 Rapid Growth Effects on Lattice Strain Model Parameterizations

Lattice strain parameters D_o, r_o, and E from the crystal chemical partitioning model of Blundy and Wood (1994) have been calculated using the divalent element partition coefficients of SrO and BaO from the 20 °C/hr cooling experiment data and compared with partitioning behavior observed for the 2 °C/hr cooling experiments, as reported in Table 2.3 of section 2.3.1. Parameter fitting follows procedures described in Section 2.3.4 using the NMinimize function of Mathematica, which employ Nelder-Mead solution methods for non-linear equations.

Table A3.8. Lattice strain parameterizations for compositions 2b-1, 2b-4, and 2b-7 under 2 °C/hr and 20 °C/hr cooling conditions using the molar partition coefficient data for SrO and BaO from Table A3.3.1 and that of CaO from chapter 2.

		D_o	E (GPa)	r_o (Å)
2 °C/hr	2b-1	0.961	107.5	1.217
	2b-4	1.173	109.6	1.209
	2b-7	1.652	111.4	1.200
20 °C/hr	2b-1	1.014	99.5	1.229
	2b-4	1.278	115.7	1.218
	2b-7	1.807	112.2	1.214
Effect of increasing cooling rate by factor of 10, from 2 °C/hr to 20 °C/hr, on parameterization:				
	2b-1	+ 5.5 %	- 7.4 %	+ 1 %
	2b-4	+ 9.0 %	+ 5.6 %	+ 0.8 %
	2b-7	+ 9.4 %	+ 0.7 %	1.1 %

Because D_{MgVIII} values have not been experimentally determined, 2 °C/hr and 20 °C/hr cooling data parameterizations are restricted in this section to SrO, BaO, and CaO, assuming that CaO partitioning behavior will be identical for both thermal regimes. Since only three partition coefficients are used to fit three parameters, the resulting Onuma curves have no misfit. The calculated parameters are listed in Table A3.8, which indicates that the greatest influence the slightly higher partition coefficients of the 20 °C/hr cooling experiments have on crystal chemical model parameters is elevating the D_o value. This effect is modest: within 10% of the 2 °C/hr cooling values. Effects on the strain parameter E are non-systematically variable, and changes in r_o are minimal.

D vs. ionic radius plots of these data are shown in Figure A3.13. Bulk magnesium partition coefficients are plotted at the ionic radius of Mg in cubic coordination (0.89 Å) (Shannon, 1976) but were not part of the curve parameterizations.

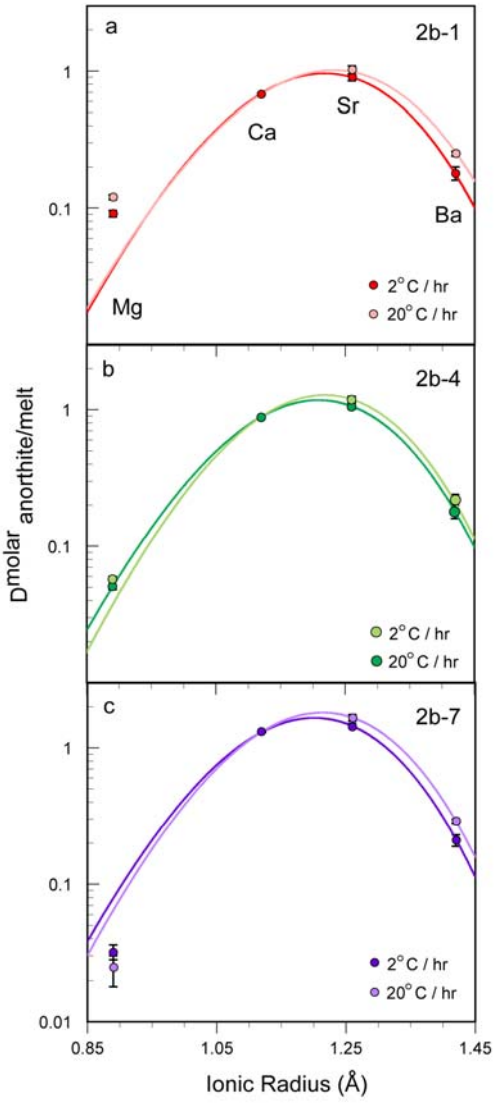

Figure A3.13. *D* vs. ionic radius curve parameterizations of Table A3.8 from 2 °C/hr and 20 °C/hr cooling data for compositions (a) 2b-1, (b) 2b-4, and (c) 2b-7. Partition coefficient 1 σ uncertainty is within symbol size except where shown.